Supporting Information

Controlling NIR-II emitting gold organic/inorganic nanohybrids with tunable morphology and surface PEG density for dynamic visualization of vascular dysfunction

Tingyao Zhou,‡[ab] Menglei Zha,‡[a] Hao Tang,[a] Kai Li,[a] and Xingyu Jiang *[a]

[a] Shenzhen Key Laboratory of Smart Healthcare Engineering, Guangdong Provincial Key Laboratory of Advanced Biomaterials, Department of Biomedical Engineering. Southern University of Science and Technology, No. 1088 Xueyuan Rd., Nanshan District, Shenzhen, Guangdong 518055, P. R. China.

[b] Institute for Advanced Study, Shenzhen University, Shenzhen, Guangdong 518060, P. R. China.

‡T. Z. and M. Z. contributed equally to this work.

* Address correspondence to: jiang@sustech.edu.cn (X. Y. Jiang)

Experimental Section

Chemicals and materials

Pluronic F127 was purchased from Sigma-Aldrich. 1, 4-butanedithiol (4C, 98%), pentaerythritol tetrakis 3-mercaptopropionate (S_4, 95%), and gold chloride hydrate were from Meryer. Sodium borohydride was from Aladdin. These agents were used as received without further purification. The cellulose membrane dialysis tubing (MWCO, 14 kDa) was from Sangon Biotech.

Animals

The female BALB/C mice and BALB/C nude mice were from Beijing Vital River Laboratory Animal Technology Co., Ltd., and housed in the Laboratory Animal Center of Southern University of Science and Technology. All animal experiments were performed in compliance with the relevant laws and institutional guidelines. All procedures for animal studies were conducted according to the approved protocols by the Institutional Animal Care and Use Committee of the Southern University of Science and Technology (SUSTech-JY2020103058). Informed consent was obtained for any experimentation with human subjects.

Optical characterization

The absorption spectra were collected using a UV-Vis spectrophotometer (UV-2600, Shimadzu, Japan). The luminescence spectra were obtained from a luminescent spectrometer (iHR320, Horiba, Japan) with an 808 nm laser as the excitation light. Lifetime measurement was performed from time-resolved photoluminescence spectroscopy (FLS1000, Edinburgh, UK) using pulsed 808 nm laser diodes as the excitation source. Ex vivo NIR-II images were carried out by an imaging system (NIROptics Series III 900/1700, Suzhou, China) with an 808 nm laser.

Structural characterization

X-ray photoelectron spectroscopy (XPS) was obtained from a K-alpha instrument (Thermo Fisher, UK) equipped with an excitation source a Mono Al Kα X-ray

radiation (1486.6 eV). Ar^+ sputtering was employed to identify the in-depth chemical states of nanomaterials, and C 1s (284.8 eV) was applied as the reference data to calibrate all the binding energies.

TEM images were collected on a Tecnai F30 TEM (Philips-FEI, Netherlands) at an accelerating voltage of 300 kV. High angle annular dark-field scanning transmission electron microscopy (HAADF-STEM) image and elemental mapping were captured from a Talos F200X TEM (FEI, USA) equipped with an energy dispersive spectroscopy (EDS) system at an accelerating voltage of 200 kV. The samples were diluted 15-fold with water, and then a drop of the samples (4 μl) was put on an ultrathin carbon grid and naturally dried after being wiped by filter paper. The ultrathin carbon grid containing the sample was entrapped by a cryo transfer tomography holder (Fischione, model 2550) for HAADF-STEM and elemental mapping experiments.

Cyto-TEM images were collected using a Titan Krios G3i instrument (Thermo Fisher, UK) operating at 300 kV equipped with a Ceta camera. The samples were diluted 3-fold with water, and a drop of the samples (4 μl) was placed on a freshly glow-discharged ultrathin carbon grid. After being blotted for 4.5 s at 4 ^oC with 100 humidity, the grid was flash-plunged in liquid ethane and then transferred to liquid nitrogen using a Vitrobot Mark IV (Thermo Fisher, UK).

Atomic force microscope (AFM) was carried out from a Multimode VIII AFM instrument (Bruker, Germany). The samples were diluted 100-fold with water, and then a drop of the samples (10 μl) was put on a plasma-cleaned Si substrate and dried at room temperature in a vacuum drier.

Synthesis of necklace-like and spherical AuNHs

For a typical synthesis of necklace-like AuNHs, 0.2 g of Pluronic F127 and 13.6 μl of 4C were dissolved in 8.8 ml water under vigorous stirring. 0.8 ml of 0.1 M $HAuCl_4$ was added dropwise under magnetic stirring, and the mixed solution turned from orange-yellow to colorless. Then, 1 M NaOH was used to adjust the pH of the mixed solution to about 10 and 4 ml of 0.1 M $NaBH_4$ was added dropwise. After vigorous stirring for

3 hours, the solution was collected and dialyzed through cellulose membrane dialysis tubing (MWCO 14 kDa) against ultrapure water for 24 h.

For the preparation of spherical AuNHs, a similar process was carried out. 0.2 of Pluronic F127, 0.32 ml of 0.1 M S_4 tetrahydrofuran solution and 8.8 ml of water were mixed under vigorous stirring, 0.4 ml of 0.1 M $HAuCl_4$ was added into the above mixture. Then, 200 μl of triethylamine and 1.2 ml of 0.1 M $NaBH_4$ were added in sequence. The mixture solution was kept for 12 h and dialyzed through cellulose membrane dialysis tubing (MWCO, 14 kDa) against ultrapure water for 24 h.

Determination of Surface PEG Density

The ^1H NMR spectra were conducted using Bruker 400 REM instrument. The 1 ml of AuNHs solutions were lyophilized by an LGJ-12A freezing dryer (Foring Technology, Beijing) and suspended in 0.5 ml of D_2O with 1 wt % 3-(trimethylsilyl)-1-propanesulfonic acid, sodium salt (DSS), which was used as an internal standard. Various concentrations of PEG_{5000} in D_2O with 1 wt % DSS (0, 0.02, 0.1, 0.5 %) were measured to draw a standard curve through the peak area ratios of $\delta_{3.65}$ to $\delta_{2.90}$. The Au atom concentration of the AuNHs was detected by inductively coupled plasma mass spectrometry (ICP-MS, 7800, Agilent, USA).

For the spherical AuNP, the number of Au atoms in this NP (N_{Au}) can be calculated using this equation.

$R = r_s \cdot N_{Au}^{1/3}$, R = NP radius, r_s = Wigner-Seitz radius.

For 4C AuNHs, N_{Au}=278, the number of Au atoms in a 4C AuNH (N_{NH}) was 1738.

For S_4 AuNHs, N_{Au}=110, the number of Au atoms in an S_4 AuNH (N_{NH}) was 805.

For 4C AuNHs, a nanohybrid 's surface area (S) could be calculated as follow: $S= 0.5\pi W^2 + \pi W \cdot L = 657.21$ nm^2.

For S_4 AuNHs, a nanohybrid 's surface area (S) could be calculated as follow: $S = \pi D^2 = 530.66$ nm^2.

The PEG density [Γ], showing the number of PEG chains on the nanohybrid surface per 100 nm^2 was calculated as following equation.

$$[\Gamma]=\frac{0.5W_{PEG}\cdot N_{NH}\cdot M_{Au}}{S\cdot W_{Au}\cdot M_{PEG}}\cdot 100$$

Where W_{PEG} and W_{Au} were mass concentration of PEG chains and total Au atom; M_{PEG} and M_{Au} were molar mass of PEG chains and Au atom, respectively. W_{PEG} was detected to be 0.0448±0.0010% for the 4C AuNHs and 0.0395±0.0005% for the S_4 AuNHs. W_{Au} was detected to be 175.91±0.53 μg/ml for the 4C AuNHs and 166.90±4.67 μg/ml for the S_4 AuNHs.

According to previous work,[1] full surface mushroom coverage [Γ*] expressed the number of unconstrained PEG chains per 100 nm^2. The diameter ξ of the PEG chain occupying a surface area was calculated as follows.

$\xi = 0.076m^{0.5}$ (nm)

Thus, PEG_{4400} could form an unconstrained area with a diameter of 5.04 nm, and occupied a surface area of 19.95 nm^2, then [Γ*] was calculated to be 5.01.

Agarose gel electrophoresis

The two types of the AuNHs solution were mixed with the PBS (pH 7.4) and fetal bovine serum (FBS) to make the AuNHs solution containing 10% FBS, respectively. The above solutions were incubated at 37 °C for 30 min. After that, each sample's solution (30 μl) was mixed with 50% glycerol (3 μl), then carefully loaded into the additional wells of a 1.5% agarose gel. The gel electrophoresis was conducted at 110 V for 30 min. The NIR-II imaging of the agarose gel was carried out by an imaging system (NIROptics Series III 900/1700, Suzhou, China) with an 808 nm laser.

Cytotoxicity test

Human umbilical vein endothelial cells (HUVEC) were used to assess the cytotoxicity of the two types of AuNHs using Calcein AM and propidium iodide (PI) protocol.[2] Briefly, HUVEC lines were cultured in Dulbecco's modified Eagle's medium (DMEM) supplemented with 10% FBS and 1% penicillin/streptomycin. The cell lines were transferred into a 24-well plate with 2.5×10^5 cells/well and cultured at 37 °C in a humidified atmosphere containing 5% CO_2 for 12 h. The medium turned to DMEM

containing different concentrations of the AuNHs, such as 0, 40 μg·ml^{-1} 4C AuNHs and 40 μg·ml^{-1} S_4 AuNHs and the cell lines continued to be cultured for another 24 h. According to the standard Calcein AM /PI protocol, the live and dead cells were stained, respectively. With the appropriate bandpass filters, fluorescence images were performed on Nikon A1R SI confocal microscopy.

Hemolysis experiments

Hemolysis experiments were performed to study the erythrocytic lysis of the AuNHs and assess their biologic safety. Fresh blood was collected from female BALB/C mice (4-5 weeks old), centrifuged at 1500 rpm for 15 min and then washed three times using 0.9 % saline. The obtained erythrocyte was dissolved in 0.9 % saline to make a 4 % cell suspension. Then, different concentrations of AuNHs solution (25, 50, 100, 200 and 400 μg·ml^{-1}) were mixed with 4 % erythrocyte suspension by equal volume. Water was used as a positive control. After centrifuging at 12000 rpm for 15 min, the picture was captured, and the absorbance of the supernatant at 540 nm was also measured by a microplate reader (BioTek, USA).

Brain vascular imaging

The female BALB/C mice (4-5 weeks old) were narcotized with isoflurane and fixed on a holder for the brain NIR-II images. After i.v. injection with the 4C AuNHs (5 mg·kg^{-1}), S_4 AuNHs (5 mg·kg^{-1}) or ICG (5 mg·kg^{-1}), NIR-II images of mice brain were collected on a MARS *in vivo* imaging system (Artemis Intelligent Imaging, Shanghai, China) equipped with 1100 nm long pass (LP) filter and excitation light source 808 nm laser at different time points (5 min, 0.5, 1, 3, 5 h). The images processing was carried out on an image J software (open source).

Pharmacokinetics and bio-distribution

To estimate the pharmacokinetics of the two types of AuNHs, the female BALB/C mice (4-5 weeks old, n=3) were i.v. injected with the 4C AuNHs (5 mg·kg^{-1}) or S_4 AuNHs (5 mg·kg^{-1}). The blood samples were collected through the venous sinus of eye-orbit in

the mouse at 2, 5, 8, 15, 30 min, 1, 3, 5, 11, 24, 48 h p.i., respectively. We then accurately weighed these collected blood samples and digested them with fresh aqua regia. After that, we measured the concentrations of gold (percentage of injection dose per gram of blood, %ID·g^{-1}) by ICP-MS. To study the bio-distribution of the two types of AuNHs, we i.v. injected with the 4C AuNHs (5 mg·kg^{-1}) or S_4 AuNHs (5 mg·kg^{-1}) into female BALB/C mice (4-5 weeks old, n=3). The mice were then sacrificed at 1 h p.i., and major organs and tissues were collected and digested with fresh aqua regia. Then, we measured the concentrations of gold (%ID·g^{-1}) by ICP-MS.

Carotid thrombosis and the NIR-II imaging of thrombolysis process

The $FeCl_3$-induced vascular injury method was introduced to establish the carotid thrombosis model.[3] Briefly, the female BALB/C nude mice (10-12 weeks old) were anesthetized with an intraperitoneal injection of ketamine (100 mg·kg^{-1})/xylazine (10 mg kg^{-1}), and vet ointment was wiped on their eyes. A midline incision was carefully performed below the jaw, soft tissue was wiped out, and a left and right carotid artery fragment was isolated, respectively. The left carotid artery was used as control, while the right was covered by filter paper (5 mm × 1 mm) soaked with 6 % $FeCl_3$ for 4 min. The filter paper was removed, and PBS was used to rinse carotid arteries. For pathological analysis, the left and right carotid arteries were collected and fixed in 4% paraformaldehyde in phosphate buffer for 48 h. The fixed carotid arteries were dehydrated and embedded with paraffin and then sectioned in an orthogonal direction of the carotid arteries. The carotid arteries sections were stained by hematoxylin and eosin (H&E) for pathological analysis.

To study real-time imaging during the thrombolysis process under different doses of the thrombolytics (recombinant tissue plasminogen activator, rt-PA), the mice were placed on a holder of the imaging system and narcotized with isoflurane. First, the mice were i.v. injected with the 4C AuNHs (5 mg·kg^{-1}) to show the location of the thrombus, and then the low dose of rt-PA (100 μl, 0.015 mg·ml^{-1}) was i.v. injected into the mouse, real-time NIR-II imaging of carotid arteries was carried out to observe the thrombus state. To increase the thrombolytic effect, another dose of rt-PA (100 μl, 0.15 mg·ml^{-1})

was i.v. injected into the mouse, real-time NIR-II imaging was applied. The real-time NIR-II imaging of carotid artery was performed by a MARS *in vivo* imaging system (Artemis Intelligent Imaging, Shanghai, China) equipped with 1100 nm long pass (LP) filter and excitation light source 808 nm laser at a power density of 0.145 W/cm^2. Image J software was utilized to adjust the contrast and brightness of the NIR-II imaging photographs and fabricate the time-lapse videos.

Additional Figures and Tables

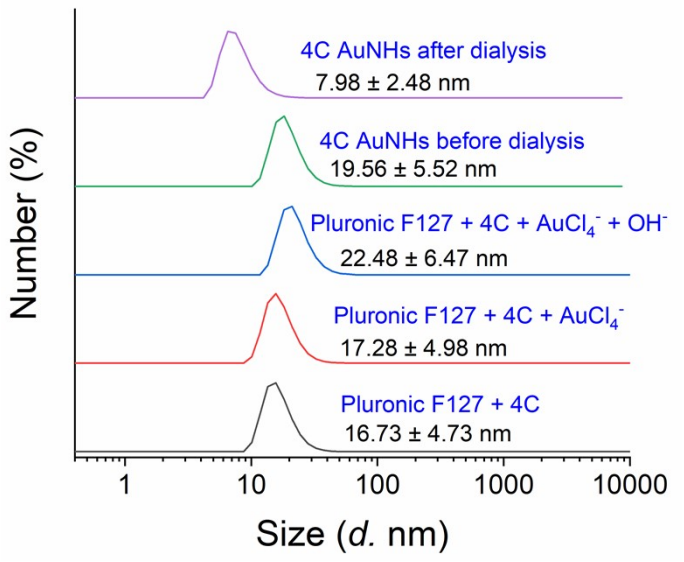

Fig. S1 The HDs of the template during the synthetic process of the 4C AuNHs.

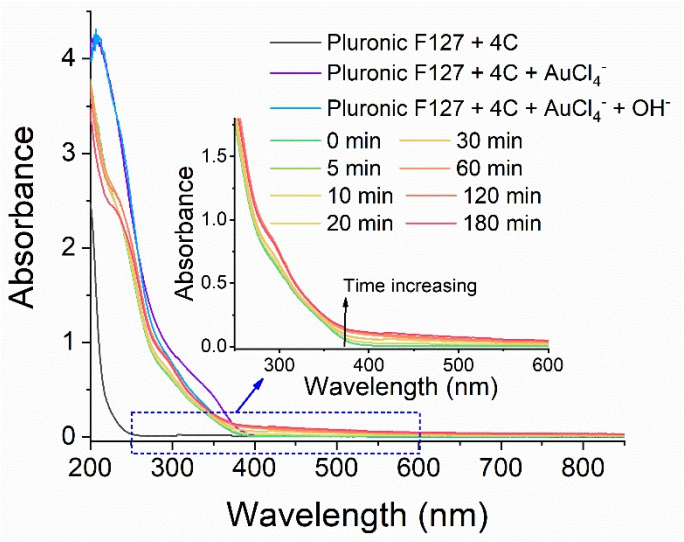

Fig. S2 UV-Vis absorption spectra of the precursors and time evolution of UV-Vis absorption spectra after adding the reductant $NaBH_4$ during the synthetic process of the 4C AuNHs.

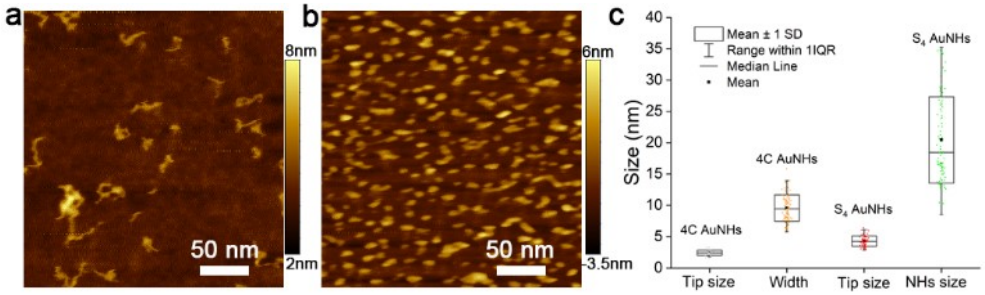

Fig. S3 AFM images of the 4C AuNHs (a) and S_4 AuNHs (b), (c) showed the tip size and lateral size distribution of the nanohybrids. The 4C AuNHs presented a linear structure with a width (lateral size) of 9.6 ± 2.0 nm and height (tip size) of 2.4 ± 0.5 nm, while the S_4 AuNHs showed a spherical shape with a lateral diameter of 20.5 ± 6.9 nm and height (tip size) of 4.3 ± 0.8 nm. Although the lateral diameters were overestimated due to the AFM tip convolution,[4] these AuNHs were flattened upon deposition on the Si substrate. This structural deformation could be attributed to several factors, including the tip force during the AFM measurement, the partial dehydration of the template, or a reconfirmation of the AuNHs on the Si substrate surface due to the hydrophobic effect.[5-7]

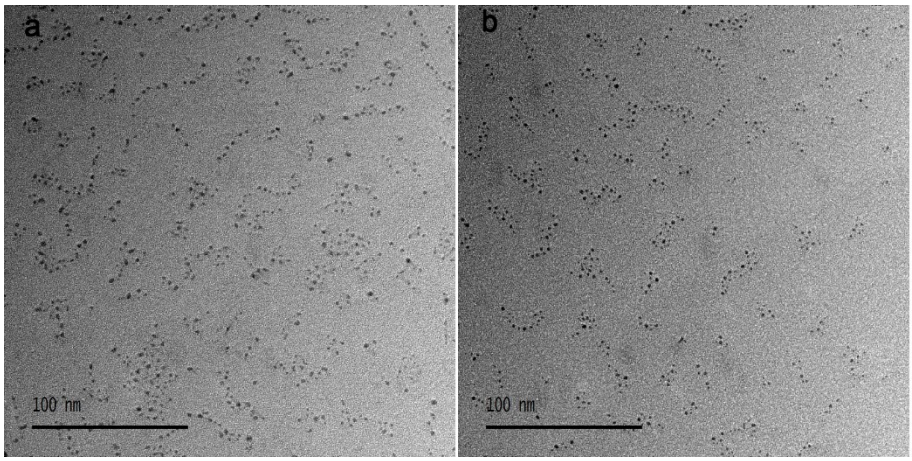

Fig. S4 TEM images of AuNHs using 1,5-pentanedithiol (5C, a) and 1,8-octanedithiol (8C, b).

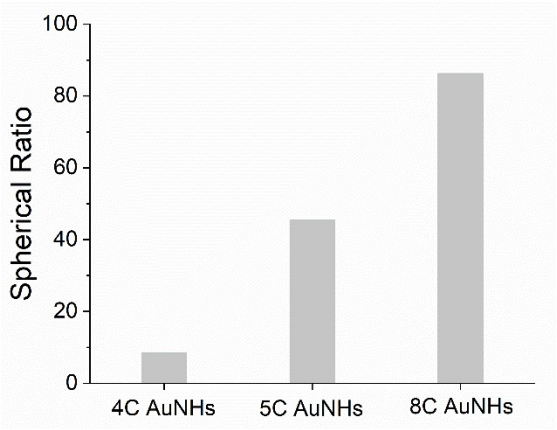

Fig. S5 The ratio of spherical assembled nanostructures from the statistics of TEM images.

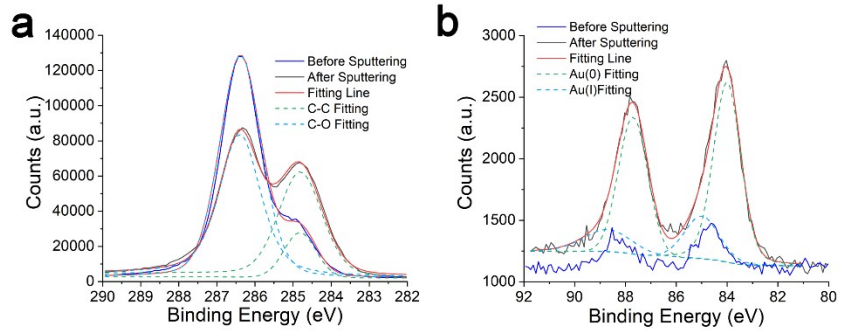

Fig. S6 C1s (a) and Au4f (b) XPS spectra of the 4C AuNHs before and after Ar^+ sputtering. The amount of Au (I) species was calculated to be 23.02 % through the peak areas' comparison.

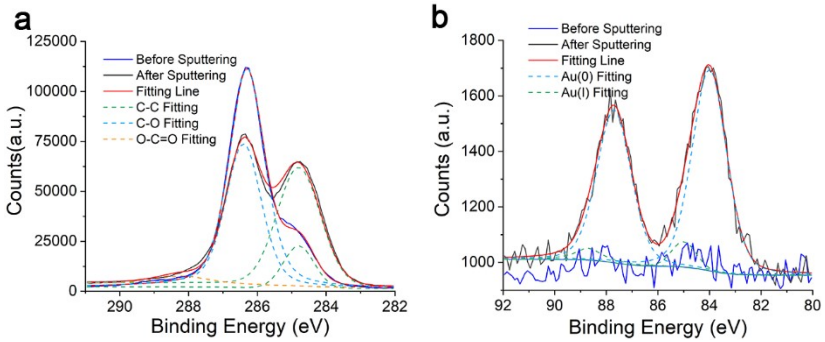

Fig. S7 C1s (a) and Au4f (b) XPS spectra of the S_4 AuNHs before and after Ar^+ sputtering. The amount of Au (I) species was calculated to be 7.4 % through the peak areas' comparison.

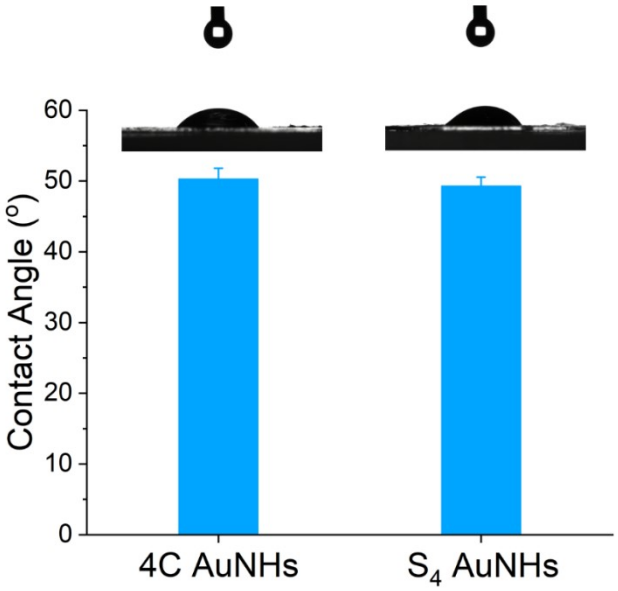

Fig. S8 Contact angle image of the 4C AuNHs and S_4 AuNHs. These particle suspensions were spined on a glass substrate to form "particle films", and then static contact angles were measured. The contact angle result thus depended on particle size and state of aggregation of NP in the films and the PEG content.[8] Meanwhile, the contact angle was only sensitive to surface chemistry with a 0.2–0.5 nm detection depth,[9] and the PEG chain was a long chain with a molecular weight of 4400. Therefore, the PEG density had little effect on the water contact angle.

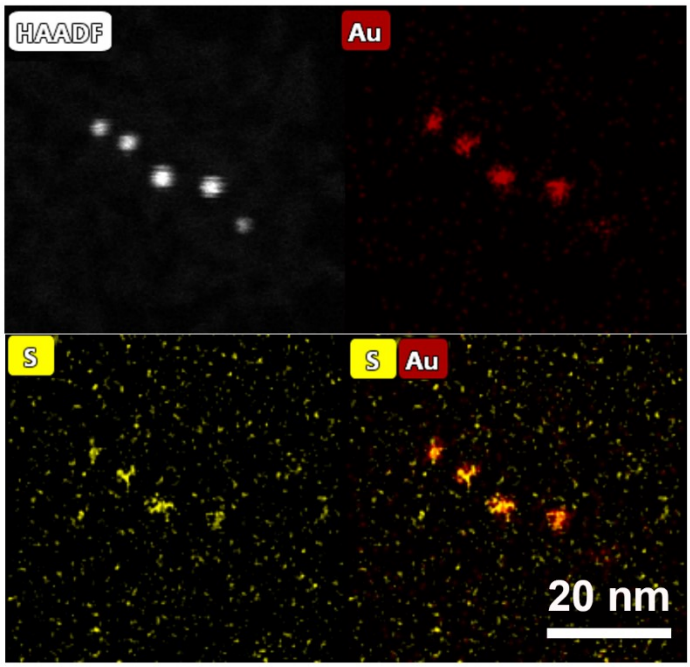

Fig. S9 HAADF-STEM image and the elemental mapping for the 4C AuNHs.

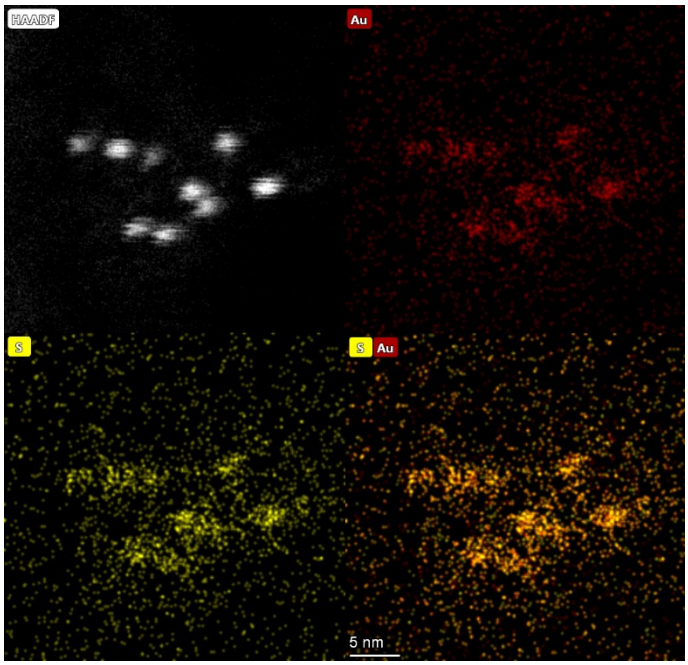

Fig. S10 HAADF-STEM image and the elemental mapping for the S_4 AuNHs.

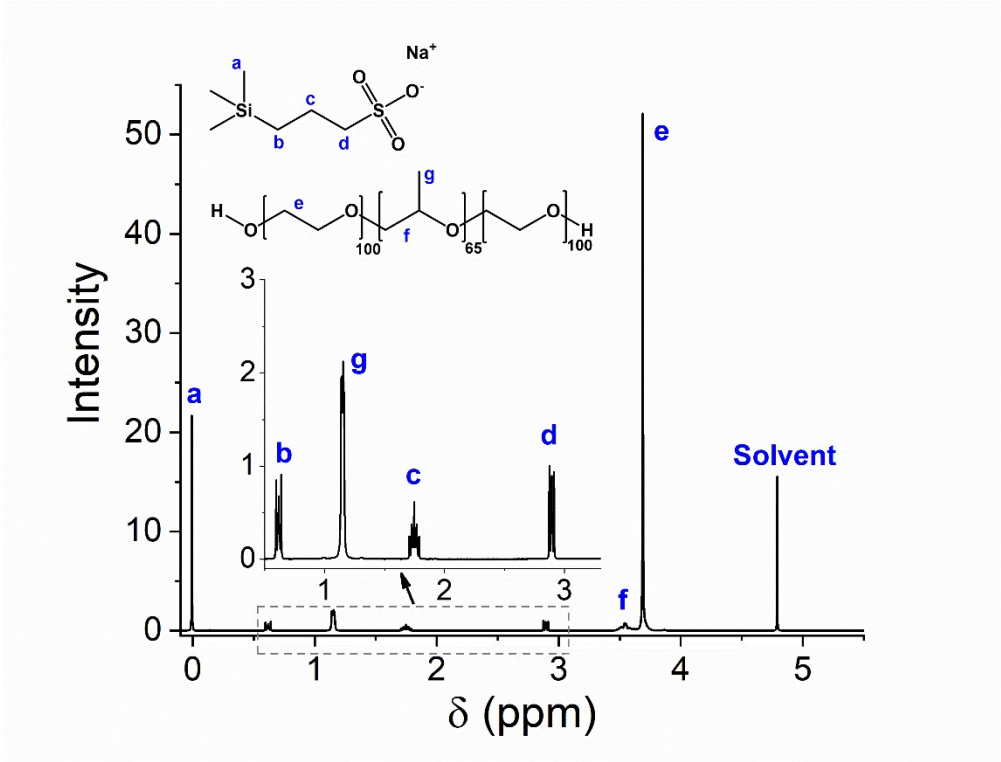

Fig. S11 ^{1}H NMR spectrum of Pluronic F127 suspended in D_2O with 1 wt % 3-(trimethylsilyl)-1-propanesulfonic acid, sodium salt (DSS). Inset showed the enlarged view of the dashed line area.

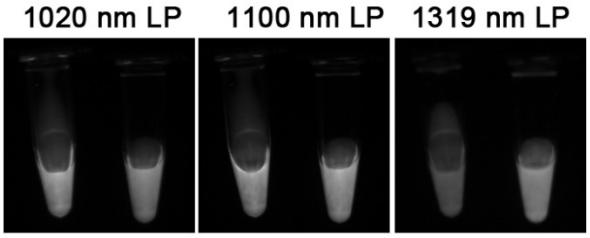

Fig. S12 Photographs of the 4C AuNHs (left) and S_4 AuNHs (right) through different long pass (LP) filters using 808 nm laser as excitation light source.

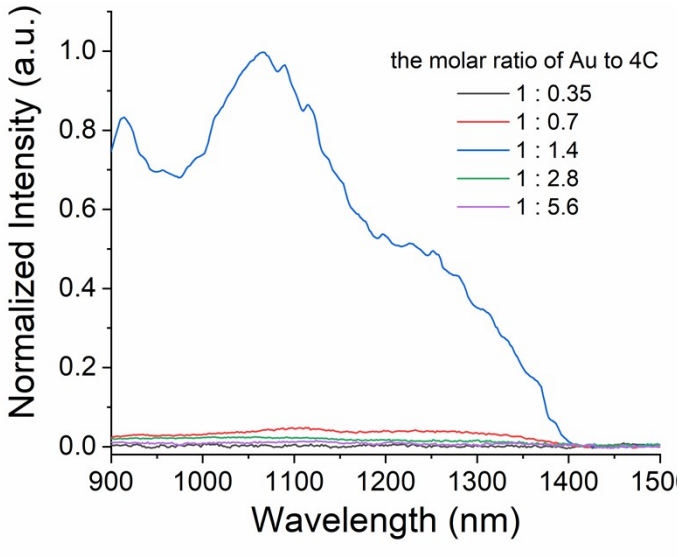

Fig. S13 NIR-II emission spectra of the AuNHs prepared by altering the different molar ratios of Au to 4C ligand.

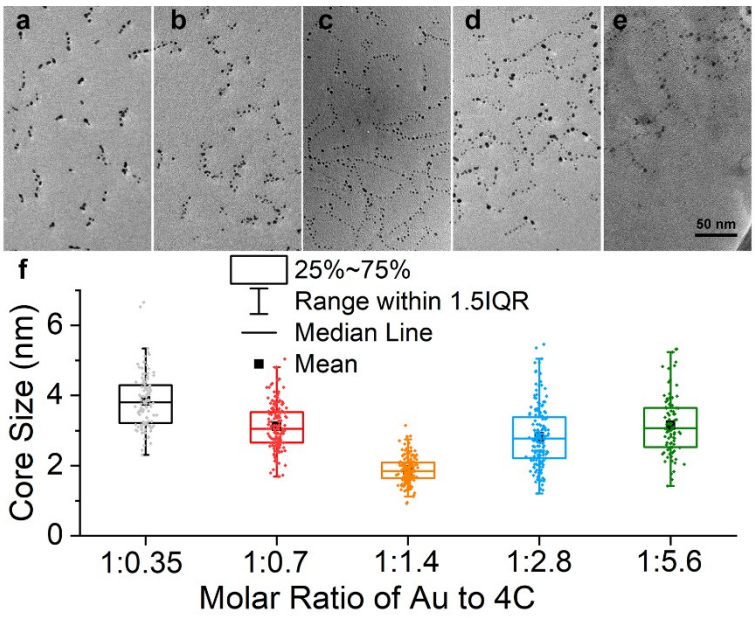

Fig. S14 TEM images of the AuNHs prepared by altering the different molar ratios of Au to 4C ligand. (a) 1:0.35; (b) 1:0.7; (c) 1:1.4; (d) 1: 2.8; (e) 1:5.6. (f) The size distribution of AuNP core of the AuNHs prepared by altering the different molar ratios of Au to 4C ligand.

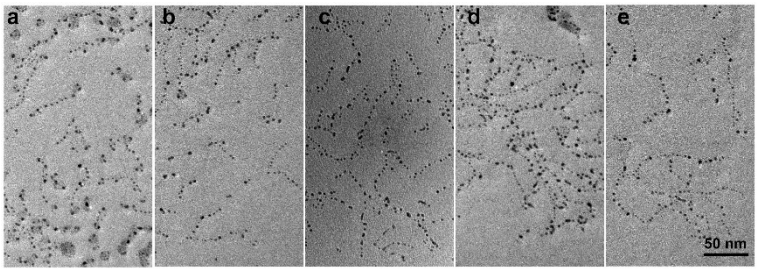

Fig. S15 TEM images of the AuNHs prepared by changing the concentrations of Pluronic F127.

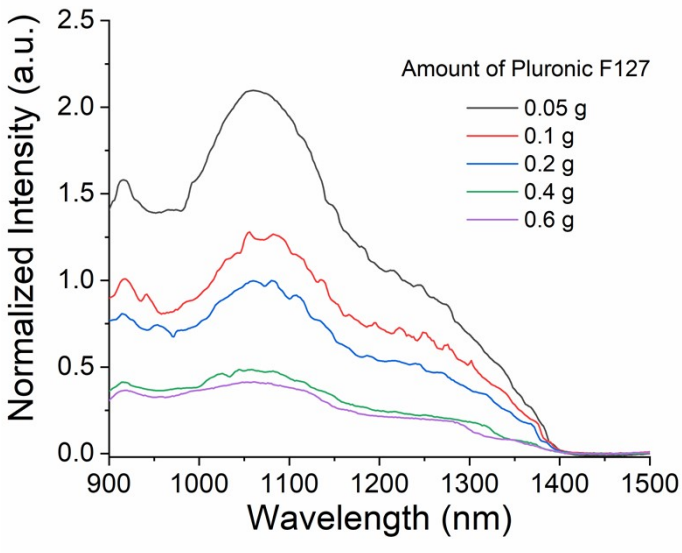

Fig. S16 NIR-II emission spectra of the AuNHs prepared by changing the concentrations of Pluronic F127.

The effects of Pluronic F127 and 4C concentrations on their NIR-II emission and assembled shape were studied. We synthesized a series of AuNHs by altering the different molar ratios of Au to 4C ligands. As shown in Fig. S13, an obvious NIR-II emission was observed only at the molar ratio of Au to 4C ligand of 1:1.4, while no NIR-II signal occurred for other molar ratios. TEM images (Fig. S14) showed that assembled shape could remain necklace-like when the molar ratio of Au to 4C ligand was less than 1:1.4. Otherwise, the formed AuNPs were large, and the assembled nanostructures changed into disorganized. As the concentrations of Pluronic F127 changed, their assembled shape remained necklace-like (Fig. S15), and the emission spectrum, including spectral shape and peak, also stayed the same except for the emission intensity. The NIR-II emission decreased as the concentrations of Pluronic F127 increased (Fig. S16). These results further demonstrated the thiol ligands 4C and

Pluronic F127 were essential in assembled shape and NIR-II emission.

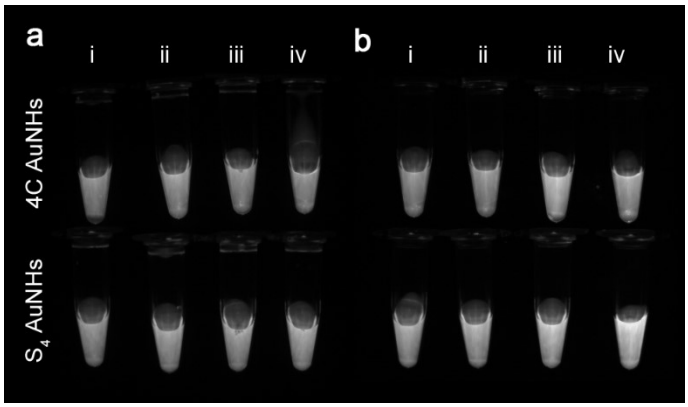

Fig. S17 Photographs of the 4C AuNHs and S_4 AuNHs in different media, such as water (i), PBS (ii), Dulbecco's Modified Eagle Medium (DMEM, iii) and DMEM supplemented with 10% FBS (iv), after being stored for 7 days at room temperature.

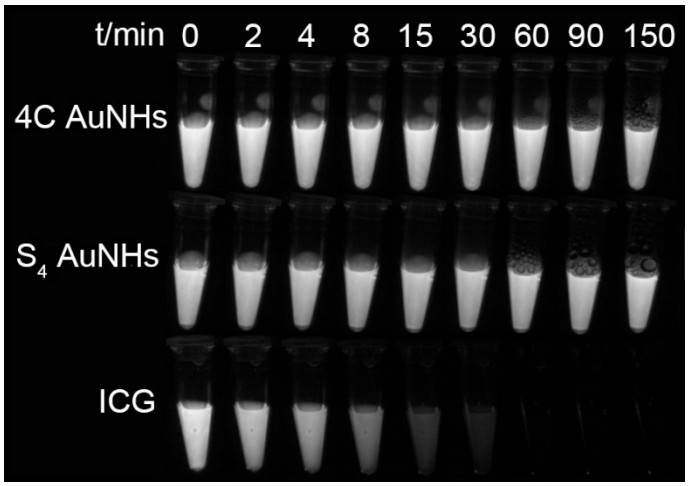

Fig. S18 Photographs in NIR-II region of the 4C AuNHs, S_4 AuNHs and ICG in water under continuous 808 nm laser irradiation for 150 min with a power density of 0.33 W/cm^2.

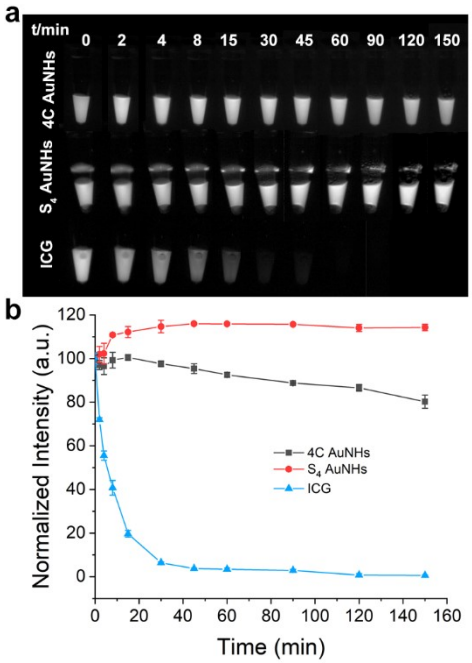

Fig. S19 Photographs in NIR-II region (a) and NIR-II emission intensity (b) of the 4C AuNHs, S_4 AuNHs, and ICG in blood under continuous 808 nm laser irradiation for 150 min with a power density of 0.33 W/cm^2. Similar to that in water, the NIR-II emissions of the two AuNHs could remain more than 80% even after irradiation for 150 min, while the signal of ICG gradually disappeared within 30 min, indicating that the two types of AuNHs also showed superior photostability in blood medium.

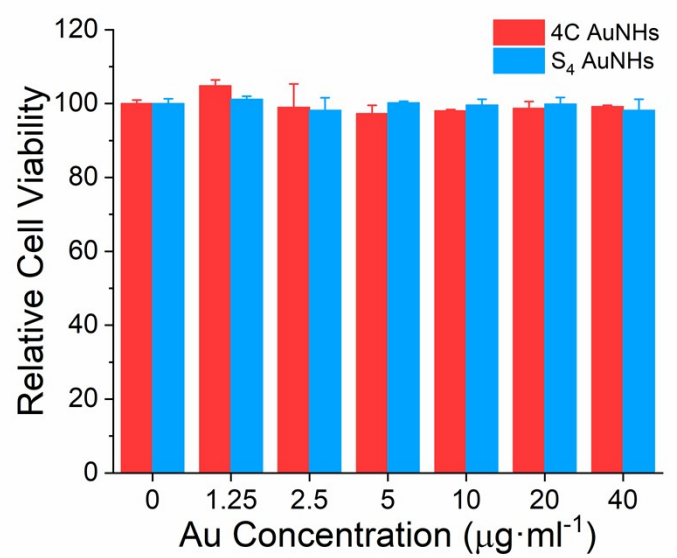

Fig. S20 Cell viability assay of the two AuNHs against HUVEC after 24 h of incubation at different Au concentrations.

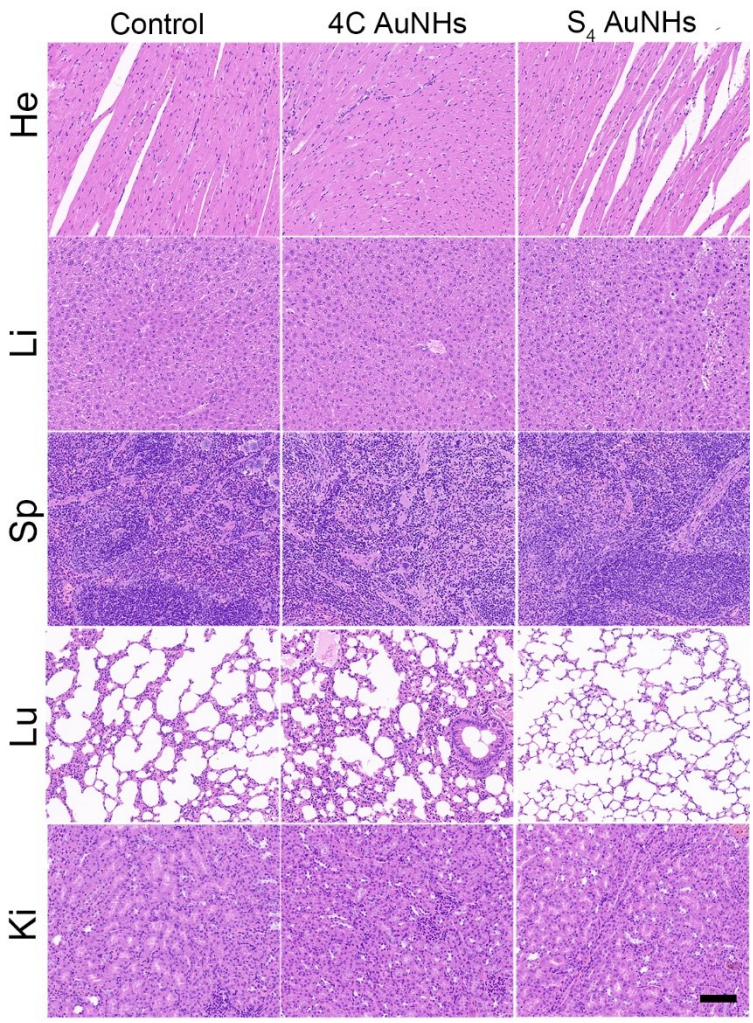

Fig. S21 Hematoxylin and eosin (H&E) staining of major organs including heart (He), liver (Li), spleen (Sp), lung (Lu), and kidney (Ki) after i.v. injection with PBS, 4C AuNHs (5 mg·kg^{-1}) and S_4 AuNHs (5 mg·kg^{-1}) for 7 days. Scale bar: 100 μm.

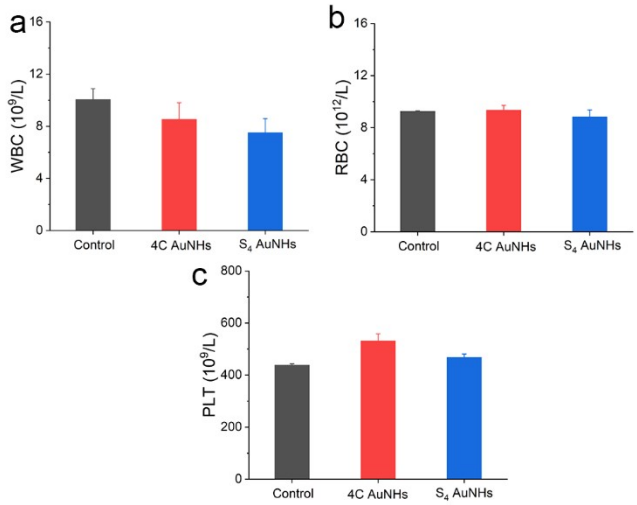

Fig. S22 Routine analysis of blood after treatment of 4C AuNHs and S_4 AuNHs at 7 days post injection.

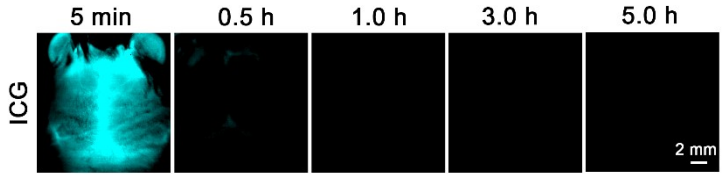

Fig. S23 NIR-II imaging of mice brain after i.v. injection with indocyanine green (ICG, 5 mg·kg^{-1}) at different time points (0.145 W/cm^2, 1100 nm LP, λ_{ex} = 808 nm, 10 ms).

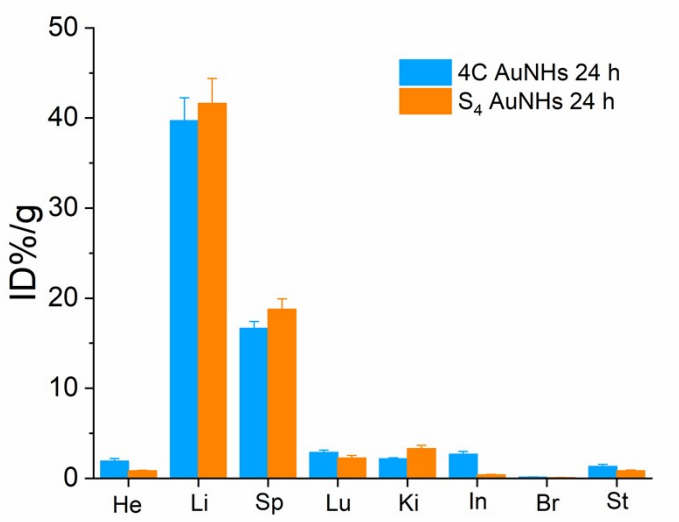

Fig. S24 The bioconcentrations of main organs and tissues were collected at 24 h post i. v. injection of the 4C AuNHs and S_4 AuNHs. He: heart, Li: liver, Sp: spleen, Lu: lung, Ki: kidney, In: intestine, Br: brain, Bo: bone, St: stomach.

Table S1 The quantum yield (QY) of the NIR-II emitting water-soluble AuNPs and organic dyes.

Materials	λ_{em} (nm)	QY	Reference dye	Reference
$Au_{25}GS_{18}$	945/1035	0.05%	IR-26, 0.05%	[10]
CD-AuNPs	1050	0.11%	IR-26, 0.05%	[11]
$Au_{25}(P12)_x(C5)_{18-x}$	~1100	0.54%	a	[12]
Au-PC	1090	0.38%	a	[13]
LA-sulfobetaine capped Au NPs	~1000	0.6%	a	[14]
$Au_{24}CuGS_{18}$	1120	0.67%	IR-26, 0.05%	[15]
GSH-AuNPs	1050	0.27%	IR-26, 0.05%	[16]
MPTMS/PEG-AuNPs	1070	1.8%	IR-26, 0.5%	[17]
RNase-A@AuNPs	1050	1.9%	IR-26, 0.5%	[18]
FD-1080	1080	0.31%	IR-26, 0.05%	[19]
CH dyes	1055	0.3%	IR-26, 0.5%	[20]
FNIR-1072	1103	0.12%	IR-26, 0.11%	[21]
Pttc-SeBTa-NIR1125 Pdots	1115	0.18%	IR-1061, 0.59%	[22]
Pttc-SeBTa-NIR1380 Pdots	1300	0.05%	IR-1061, 0.59%	[22]
S_4 AuNHs	1070	0.11%	IR-1061, 0.59%[b]	This work
4C AuNHs	1070	0.59%	IR-1061, 0.59%	This work

a: The QY is measured using an integrated sphere technique.

b: Instead of using IR-26 as the reference dye due to the difference of its QY values on different reports, we used IR-1061 as the reference because its QY was carefully corrected for solvent and reabsorption/reemission.[22, 23]

Table S2 Lifetime values of the AuNHs obtained through biexponential curve fitting.

Materials	τ_1(μs)	τ_2(μs)	B_1(%)	B_2(%)	τ(μs)
S_4 AuNHs	1.87	7.43	97.54	2.46	2.00
4C AuNHs	2.50	9.83	94.49	5.51	2.90

For 4C AuNHs, due to the appropriate amount of Au (I) species (23.02 %), the rigid ligands 1, 4-butanedithiol could build an effective bridge among ultrasmall AuNPs, which can immobilize the Au core and suppress the nonradiative motions. Based on the following equations: $\tau = 1/(k_r + k_{nr})$; $QY = k_r/(k_r + k_{nr})$,[24] where k_r and k_{nr} were radiative and nonradiative, respectively, the k_r and k_{nr} of the 4C AuNHs can be calculated as 2.03×10^3 and 3.4×10^5 s^{-1}. Therefore, the enhanced luminescence of the 4C AuNHs was attributed to an efficient bridge among ultrasmall AuNPs with an appropriate amount of Au (I) species (23.02 %) and effective protection by the dense surface PEG in brush configuration.

For S_4 AuNHs, they had a smaller amount of Au(I) species (7.4%), causing a deeper color and a higher absorbance at 808 nm at the same Au atom concentration. Due to the smaller amount of Au(I) species (7.4%), they cannot build an effective bridge to immobilize the Au core and suppress the nonradiative motions. Based on the following equations: $\tau = 1/(k_r + k_{nr})$; $QY = k_r/(k_r + k_{nr})$, the k_r and k_{nr} of the S_4 AuNHs can be calculated as 0.55×10^3 and 5.0×10^5 s^{-1}. Compared with the 4C AuNHs, the nonradiative decay was enhanced for the S_4 AuNHs due to the smaller amount of Au(I) species (7.4%) and the lower surface PEG coverage.

Table S3 The blood half-life and areas under curves (AUC) of the previous reported small AuNPs.

Materials	**blood half-life (min)**	**AUC (% ID·h·g^{-1})**	**Determination method**	**Reference**
$Au_{25}GS_{18}$	<2	-	ICP-MS	[25]
AuMHA/TDT	25.8	-	ICP-MS	[26]
$AuZwMe_2$	6.5	-	ICP-MS	[25]
GSH-AuNPs	5.4	47.2	ICP-MS	[27]
PEG-AuNPs	56.1	142.8	ICP-MS	[27]
S_4 AuNHs	10	114.52	ICP-MS	This work
4C AuNHs	206.4	301.66	ICP-MS	This work

References

1. D. T. Auguste, S. P. Armes, K. R. Brzezinska, T. J. Deming, J. Kohn and R. K. Prud'homme, *Biomaterials*, 2006, **27**, 2599-2608.
2. L. L. Y. Chan, K. J. McCulley and S. L. Kessel, *Cell Viability Assays: Methods and Protocols*, Gilbert, D. F., Friedrich, O. Eds.; Springer New York, 2017; pp 27-41.
3. T. Bonnard and C. E. Hagemeyer, *J. Vis. Exp.*, 2015, **100**, e52838.
4. Y. Ebenstein, E. Nahum and U. Banin, *Nano Lett.*, 2002, **2**, 945-950
5. K. J. Wilkinson, E. Balnois, G. G. Leppard and J. Buffle, *Colloids Surf., A,* 1999, **155**, 287-310.
6. Y. Shan, N. Panday, Y. Myoung, M. Twomey, X. Wang, W. Li, E. Celik, V. Moy, H. Wang, J. H. Moon and J. He, *Macromol. Biosci.,* 2016, **16**, 599-607.
7. C. Feng, X. Pang, Y. He, B. Li and Z. Lin, *Chem. Mater.*, 2014, **26**, 6058-6067.
8. J.-M. Rabanel, P. Hildgen and X. Banquy, *J. Control Release*, 2014, **185**, 71-87.
9. C. D. Bain and G. M. Whitesides, *J. Am. Chem. Soc.*, 1988, **110**, 5897-5898.
10. Y. Yang, Y. Yu, H. Chen, X. Meng, W. Ma, M. Yu, Z. Li, C. Li, H. Liu, X. Zhang, H. Xiao and Z. Yu, *ACS Nano*, 2020, **14**, 13536-13547.
11. X. R. Song, W. Zhu, X. G. Ge, R. F. Li, S. H. Li, X. Chen, J. B. Song, J. P. Xie, X.

Y. Chen and H. H. Yang, *Angew. Chem., Int. Ed.*, 2021, **60**, 1306-1312.

12. Z. Pang, Q. Li, Y. Jia, W. Yan, J. Qi, Y. Guo, F. Hu, D. Zhou and X. Jiang, *Chem. Sci.*, 2021, **12**, 14871-14882.
13. A. Baghdasaryan, F. Wang, F. Ren, Z. Ma, J. Li, X. Zhou, L. Grigoryan, C. Xu and H. Dai, *Nat. Commun.*, 2022, **13**, 5613.
14. Y. Chen, D. M. Montana, H. Wei, J. M. Cordero, M. Schneider, X. Le Guével, O. Chen, O. T. Bruns and M. G. Bawendi, *Nano Lett.*, 2017, **17**, 6330-6334.
15. H. Liu, G. Hong, Z. Luo, J. Chen, J. Chang, M. Gong, H. He, J. Yang, X. Yuan, L. Li, X. Mu, J. Wang, W. Mi, J. Luo, J. Xie and X. D. Zhang, *Adv. Mater.*, 2019, **31**, e1901015.
16. D. Li, Q. Liu, Q. Qi, H. Shi, E. C. Hsu, W. Chen, W. Yuan, Y. Wu, S. Lin, Y. Zeng, Z. Xiao, L. Xu, Y. Zhang, T. Stoyanova, W. Jia and Z. Cheng, *Small*, 2020, **16**, e2003851.
17. K. Zhou, W. Cai, Y. Tan, Z. Zhao and J. Liu, *Angew. Chem., Int. Ed.*, 2022, **61**, e202212214.
18. W. Wang, Y. Kong, J. Jiang, Q. Xie, Y. Huang, G. Li, D. Wu, H. Zheng, M. Gao, S. Xu, Y. Pan, W. Li, R. Ma, M. X. Wu, X. Li, H. Zuilhof, X. Cai and R. Li, *Angew. Chem., Int. Ed.*, 2020, **59**, 22431-22435.
19. B. Li, L. Lu, M. Zhao, Z. Lei and F. Zhang, *Angew. Chem., Int. Ed.*, 2018, **57**, 7483-7487.
20. A. L. Antaris, H. Chen, K. Cheng, Y. Sun, G. Hong, C. Qu, S. Diao, Z. Deng, X. Hu, B. Zhang, X. Zhang, O. K. Yaghi, Z. R. Alamparambil, X. Hong, Z. Cheng and H. Dai, *Nat. Mater.*, 2016, **15**, 235-242.
21. V. G. Bandi, M. P. Luciano, M. Saccomano, N. L. Patel, T. S. Bischof, J. G. P. Lingg, P. T. Tsrunchev, M. N. Nix, B. Ruehle, C. Sanders, L. Riffle, C. M. Robinson, S. Difilippantonio, J. D. Kalen, U. Resch-Genger, J. Ivanic, O. T. Bruns and M. J. Schnermann, *Nat. Methods*, 2022, **19**, 353-358.
22. M. H. Liu, Z. Zhang, Y. C. Yang and Y. H. Chan, *Angew. Chem., Int. Ed.*, 2021, **60**, 983-989.
23. R. Hoshi, K. Suzuki, N. Hasebe, T. Yoshihara and S. Tobita, *Anal. Chem.*, 2020,

92, 607-611.

24. Q. Li, C. J. Zeman, G. C. Schatz and X. W. Gu, *ACS Nano*, 2021, **15**, 16095-16105.
25. Z. Yu, B. Musnier, K. D. Wegner, M. Henry, B. Chovelon, A. Desroches-Castan, A. Fertin, U. Resch-Genger, S. Bailly, J. L. Coll, Y. Usson, V. Josserand and X. Le Guével, *ACS Nano*, 2020, **14**, 4973-4981.
26. X. Le Guével, M. Henry, V. Motto-Ros, E. Longo, M. I. Montañez, F. Pelascini, O. de La Rochefoucauld, P. Zeitoun, J.-L. Coll, V. Josserand and L. Sancey, *Nanoscale*, 2018, **10**, 18657-18664.
27. J. Liu, M. Yu, X. Ning, C. Zhou, S. Yang and J. Zheng, *Angew. Chem., Int. Ed.*, 2013, **52**, 12572-12576.